Volume 54
Number 24
28 June 2025
Pages 9429-9790

Dalton Transactions

An international journal of inorganic chemistry

rsc.li/dalton

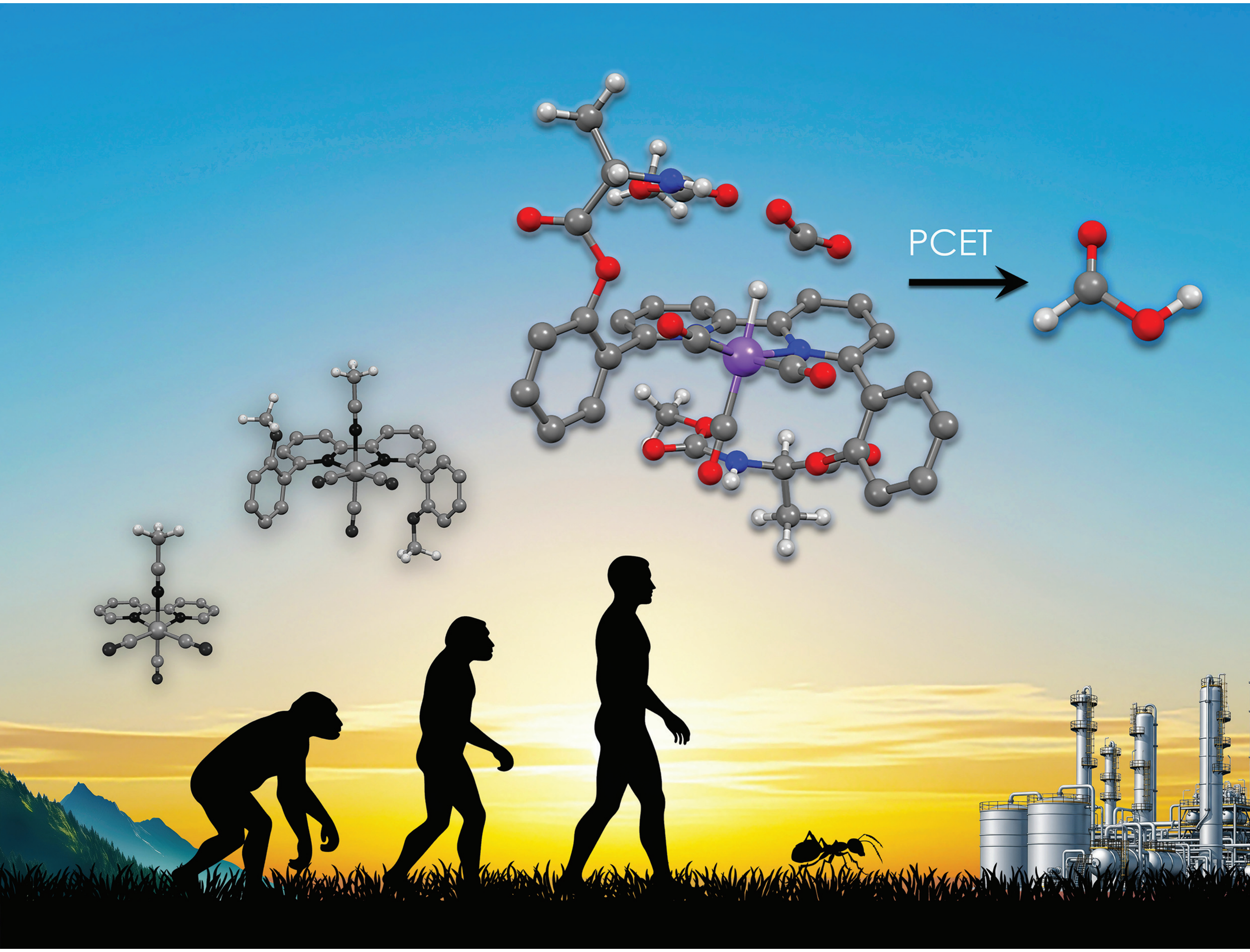

ISSN 1477-9226

ROYAL SOCIETY OF CHEMISTRY

PAPER

Jonathan Rochford *et al.*

The impact of second coordination sphere functional group extension on product selectivity for manganese bipyridyl CO_2 reduction electrocatalysts

Acknowledgement: Image created with Google Gemini AI

Dalton Transactions

PAPER

View Article Online
View Journal | View Issue

Cite this: *Dalton Trans.*, 2025, **54**, 9494

The impact of second coordination sphere functional group extension on product selectivity for manganese bipyridyl CO_2 reduction electrocatalysts†

Lisa Suntrup,[a] Vanna Blasczak,[a] Roonak Saeedi,[a] Mehmed Z. Ertem[b] and Jonathan Rochford *[a]

Received 20th January 2025,
Accepted 20th May 2025

DOI: 10.1039/d5dt00157a

rsc.li/dalton

Utilizing the well established manganese bipyridyl class of homogeneous electrocatalyst, four new ligands are studied to probe the influence of distal, outer coordination sphere, H-bonding and steric effects on product selectivity for proton-coupled electrocatalytic CO_2 reduction. The presence of a simple acetate functional group in the second coordination sphere provides a high selectivy for CO_2-to-CO conversion irrespective of proton source (H_2O *vs.* PhOH) or applied potential. The *o*-(methoxybenzoate)phenyl second/outer coordination sphere at the bipyridyl 6,6′-positions imparts poor product selectivity. In contrast, upon conjugation of the acetate functional group with the *N*-Boc-alanine moiety, a CO : HCO_2^- product selectivity of ~1 : 1 is observed at the high overpotential catalytic wave (for both H_2O and PhOH acids). Computed enthalpy and free energy of activation parameters suggest that selective CO_2 insertion at the manganese hydride transition state is favored, over protonation, consistent with negligible hydrogen production during controlled potential electrolysis studies.

Introduction

The [Ni–Fe]CODH enzyme has inspired many studies of molecular transition metal catalyst designs for electrocatalytic CO_2 reduction,[1–3] in particular toward the role of secondary and outer coordination sphere effects on enhancing catalytic performance.[4–7] By extending the second coordination sphere functionality one can potentially mimic the qualities of enzymatic co-factors and allosteric effects found in nature by including extended hydrogen bonding (H-bonding) networks, and through-space electrostatic effects. This strategy has seen successful application in electrocatalytic proton,[8–10] CO_2 [11–24] and CO[25] reduction as well as CO_2 hydrogenation[26–32] catalysis. One of the first studies highlighting the role of the outer coordination sphere was for the purpose of electrocatalytic H_2 oxidation where $[Ni^{II}(P^{Cy}{}_2N^{Gly}{}_2)_2]^{2+}$ catalysts (where P_2N_2 = 1,5-diaza-3,7-diphosphacyclooctane) were functionalized with glycine. This was found to facilitate proton transfer from the outer carboxylate groups to the pendant amino groups in the second coordination sphere, enabling electrocatalytic H_2 oxidation over a wide range of pH values (0.1–9.0).[33] The outer coordination sphere of a homogenous transition metal complex is understandably less well defined than the inner and second coordination spheres. An outer coordination sphere may take the form of bulk solvent and electrolyte and any co-factors dissolved therein, each of which can potentially participate with the inner and second coordination sphere of a transition metal complex along its reaction coordinate.[19,22,34,35] For example, the 1-ethyl-3-methylimidazolium tetracyanoborate, [EMIm][TCB], ionic liquid electrolyte was found to increase the rate of CO_2 to CO reduction for the [*fac*-ReCl(2,2′-bipyridine)$(CO)_3$] pre-catalyst at a reduced overpotential through an outer sphere $[EMIm]^+|bpy^{\bullet-}$ π-stacking interaction.[12] Gotico *et al.* later demonstrated a similar rate enhancement upon covalently incorporating a urea second coordination sphere at an Fe(III)Cl *meso*-tetraphenylporphyrin pre-catalyst.[17] This was later attributed to multipoint hydrogen-bond templating of the bicarbonate anion in the second coordination sphere at the rate-determining C–OH bond-cleavage transition state.[36] Also noteworthy is how Liu and McCrory encapsulated the cobalt phthalocyanine (CoPc) complex within a hydrophobic poly-4-vinylpyridine (P4VP) membrane thereby increasing CO product selectivity through optimized proton delivery in the outer coordination

[a]*Department of Chemistry, University of Massachusetts Boston, 100 Morrissey Boulevard, Boston, MA 02125, USA. E-mail: jonathan.rochford@umb.edu*
[b]*Chemistry Division, Brookhaven National Laboratory, Upton, New York 11973-5000, USA*

† Electronic supplementary information (ESI) available: Synthesis, HRMS and NMR data, additional voltammetry and IRSEC data, computed geometries. See DOI: **https://doi.org/10.1039/d5dt00157a**

sphere.[18,37] Williams *et al.* similarly enhanced CO_2 reduction rates by introducing triazolium proton relays at the periphery of a related zinc porphyrin catalyst.[20] It should never be overlooked, however, that second and outer coordination sphere effects at any catalytically active transition metal site are primarily dependent upon the core catalyst itself, *i.e.* the active metal site and its inner coordination sphere; and in the case of proton-coupled electron transfer (PCET) based catalysts, the proton donor activity and its transition state participation play another key role. In particular, group VII Mn(I) and Re(I) polypyridyl tricarbonyl catalysts have played a pivotal part in the study of second coordination sphere effects for CO_2 reduction.[38–59] The four Mn(I) bipyridyl tricarbonyl complexes presented in this study each contain an *ortho*-arylester second coordination sphere functional group at the 6,6′-positions of a $[fac\text{-}Mn^I(R_2\text{-bpy})(CO)_3(CH_3CN)]^+$ pre-catalyst. This is inspired by our prior work that established the capability of an *ortho*-arylether second coordination sphere at promoting the low overpotential protonation-first pathway for electrocatalytic CO_2 to CO conversion by this highly popular class of homogenous molecular catalyst.[43] Switching to the *o*-arylester second coordination sphere maintains this low overpotential catalyst activation, whilst also allowing for facile extension beyond the second coordination sphere functionality. In reference to the *o*-phenylacetate substituted bpy ligand of **[1-CH$_3$CN]$^+$**, the *tert*-butyloxycarbonyl protected alanine (*N*-boc-ala) and *o*-methoxybenzoate groups of pre-catalysts **[2-CH$_3$CN]$^+$** and **[3-CH$_3$CN]$^+$**, were here chosen to investigate how extension of the second coordination sphere H-bonding environment impacts the thermodynamic and kinetic performance of the catalyst as well as its product selectivity (Chart 1). The 2,6-dimethylphenylester group was also studied in **[4-CH$_3$CN]$^+$** to probe any steric influence extending from the *o*-arylester second coordination sphere in this series of catalysts. It is important to note that, due to functionalization of the 6,6′-phenyl rings of the bpy ligands at just a single *ortho*-position, upon coordination at Mn a mixture of *syn*,*syn*, *syn*,*anti* and *anti*,*anti* atropisomers are possible with respect to the stereochemistry of the *o*-phenyl substituents and the Mn–CH_3CN site where CO_2 and H^+ binding, and catalytic activity is anticipated to occur.

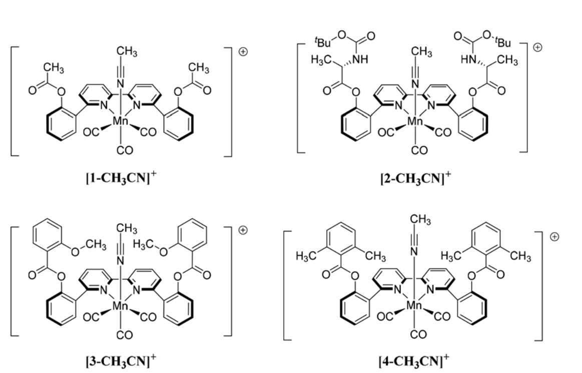

Chart 1 Manganese(I) facial tricarbonyl pre-catalyst complexes with 6,6′-substituted 2,2′-bipyridine ligands used in this study. For brevity, only the *syn*,*syn*-atropisomers are drawn.

Results

Synthesis

All 6,6′-disubstituted bipyridine ligands are previously unreported and prepared by conducting Steglich esterification on the 6,6′-bis(2-hydroxyphenyl)-2,2′-bipyridine intermediate using dicyclohexyl carbodiimide (DCC) and 4-dimethylaminopyridine (DMAP) with either acetic acid, *N*-boc-alanine, *o*-methoxybenzoic acid or 2,6-dimethylbenzoic acid in dichloromethane solvent at room temperature (Scheme 1).

Synthesis of the $[fac\text{-}Mn^I(OTf)(N^\wedge N)(CO)_3]$ complexes was conducted following a previously published procedure where freshly prepared $[Mn^I(OTf)(CO)_5]$ and the respective ligand were heated in weakly coordinating THF to give the target compounds in good yields.[43] A full description of all synthetic procedures is provided in the ESI.† Once dissolved in acetonitrile, the weakly coordinating triflate anion is displaced by a solvent molecule, thus all complexes are forthwith referred to as **[1-CH$_3$CN]$^+$**, **[2-CH$_3$CN]$^+$**, **[3-CH$_3$CN]$^+$** and **[4-CH$_3$CN]$^+$**. As discussed above, a mixture of atropisomers are likely with respect to the stereochemical location of the *o*-phenyl substituents and the Mn–CH_3CN solvation site where CO_2 binding at catalytic activity is anticipated to occur. This is evident in the ^1H NMR spectra of all Mn complexes. For example, the terminal methyl moieties of the acetate groups in **[1-CH$_3$CN]$^+$** appears as two closely spaced singlets (ESI Fig. 7†), the alanine –NH and –CH protons in **[2-CH$_3$CN]$^+$** appear as multiplets (ESI Fig. 10†), while the spectra for the bulkier **[3-CH$_3$CN]$^+$** and **[4-CH$_3$CN]$^+$** appear broad an unresolved (ESI Figs. 13 and 16†).

FTIR spectroscopy

Each of the $[fac\text{-}Mn(N^\wedge N)(CO)_3(CH_3CN)]^+$ solvated complexes exhibit almost identical ν(C≡O) IR absorption bands, characteristic of the *fac*-tricarbonyl manganese core, with a symmetric stretch at 2044 cm^{-1} and a broad asymmetric ν(C≡O) stretch at lower wavenumber 1957–1958 cm^{-1}. **[1-CH$_3$CN]$^+$** appears to impart a slight descent in symmetry from a C_3 to C_s point group as its low wavenumber ν(C≡O) band is almost resolved into two individual peaks evident at 1958 and 1949 (sh) cm^{-1}. Characteristic ν(C═O) stretches of each *o*-arylester group at the bpy ligands are also observed for all four complexes. **[1-CH$_3$CN]$^+$** exhibits a ν(C═O) stretch at 1768 cm^{-1}, with a shoulder at 1752 cm^{-1}. A similar absorption profile is exhibited by **[3-CH$_3$CN]$^+$** at 1747 and 1729(sh) cm^{-1}, and **[4-CH$_3$CN]$^+$** at 1769 and 1755(sh) cm^{-1}. The shoulder observed for each of these ν(C═O) stretches is tentatively attributed to

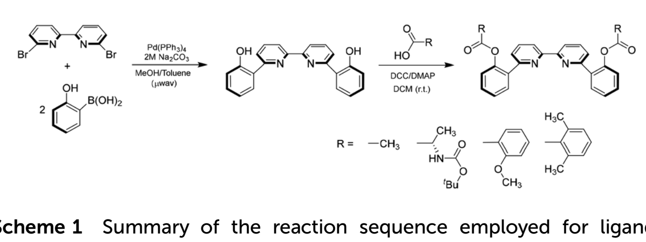

Scheme 1 Summary of the reaction sequence employed for ligand synthesis.

the presence of atropisomers as suggested also by their ^1H NMR spectra. **[2-CH$_3$CN]$^+$** is unique in that it exhibits two independent stretches at 1772 and 1713 cm^{-1} attributed to the *o*-arylester and *N*-boc ester groups, respectively.[60] FTIR spectra are illustrated in Fig. 1 and tabulated below alongside infrared spectroelectrochemical (IRSEC) data (Table 2).

Voltammetry under 1 atm Ar

We have previously established that the benchmark [Mn^I(bpy)(CO)$_3$(CH$_3$CN)]$^+$ pre-catalyst, and its 6,6′-subsituted derivatives, exhibit a two-electron activation at the first reduction wave (eqn (1)–(3)).[56] For brevity the core five-coordinate [*fac*-Mn(R$_2$bpy)(CO)$_3$] structure is abbreviated here as [Mn] with [Mn–X] indicating the variable sixth coordination site in eqn (1)–(5). The two-electron reduced [Mn^I(bpy)(CO)$_3$]$^-$ product, lacking any steric bulk, undergoes a subsequent bimolecular parent-child comproportionation chemical reaction to form the [Mn–Mn]^0 dimer (eqn (4)).[53,61] A second reduction wave occurs at −1.83 V for [Mn^I(bpy)(CO)$_3$(CH$_3$CN)]$^+$ attributed to reduction of this dimer for quantitative formation of the two-electron reduced five-coordinate 18-valence electron active catalyst [Mn]$^-$ (eqn (5)).

$$[\text{Mn–CH}_3\text{CN}]^+ + e^- \rightleftharpoons [\text{Mn–CH}_3\text{CN}]^0 \quad (1)$$

$$[\text{Mn–CH}_3\text{CN}]^0 \rightleftharpoons [\text{Mn}]^0 + \text{CH}_3\text{CN} \quad (2)$$

$$[\text{Mn}]^0 + e^- \rightleftharpoons [\text{Mn}]^- \quad (3)$$

$$[\text{Mn–CH}_3\text{CN}]^+ + [\text{Mn}]^- \rightleftharpoons [\text{Mn–Mn}]^0 + \text{CH}_3\text{CN} \quad (4)$$

$$[\text{Mn–Mn}]^0 + 2e^- \rightleftharpoons 2[\text{Mn}]^- \quad (5)$$

Consistent with prior literature, the presence of steric bulk in complexes **[1-CH$_3$CN]$^+$**–**[4-CH$_3$CN]$^+$** from their 6,6′-bpy aryl substituents prevents the comproportionation reaction (eqn (4)) mitigating any [Mn–Mn]^0 dimer formation.[43,48,56–59,62] The assignment of a two-electron reduction to the first reduction wave of all four complexes was also confirmed by IRSEC studies presented below. Scan rate dependent voltammetry of this reduction wave confirms its reversibility for **[1-CH$_3$CN]$^+$** and quasi-reversibility for the remaining complexes (ESI Fig. 17–24†). The slight negative shifts relative to the [Mn^I(bpy)(CO)$_3$(CH$_3$CN)]$^+$ pre-catalyst is consistent with an inductive donating influence of the 6,6′-bisaryl substituents raising their bpy(π*) LUMO levels by 0.07–0.08 eV. A third reduction is observed at more negative potentials. This is likely irrelevant for electrocatalysis investigations presented below, at least for complexes **[1-CH$_3$CN]$^+$** and **[2-CH$_3$CN]$^+$**. However, the positive shift of this third reduction for **[3-CH$_3$CN]$^+$** and the presence of three additional reduction peaks for **[4-CH$_3$CN]$^+$** is perhaps related to reduction of their more conjugated ester groups. This appears to have a strong impact on catalysis investigations (*vide infra*). A summary of all electrochemical data is provided in Table 1, with cyclic voltammograms recorded under non-catalytic conditions (0.1 M [Bu$_4$N][PF$_6$] acetonitrile supporting electrolyte under 1 atm of argon), presented in Fig. 2.

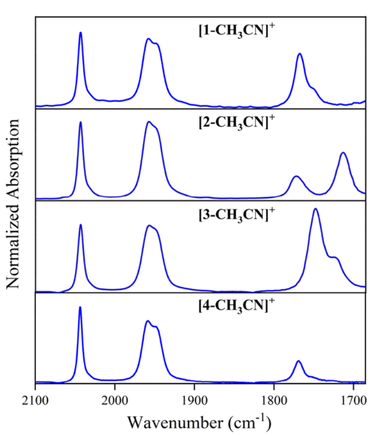

Fig. 1 FTIR absorption spectra of all four recorded in acetonitrile.

Infrared spectroelectrochemistry

IRSEC experiments were conducted to confirm the mechanism by which catalyst activation is occurring. Evidence of the six-coordinate, one-electron reduced neutral species **[1-CH$_3$CN]^0** and **[2-CH$_3$CN]^0** was observed *en route* to quantitative formation of their two-electron reduced active catalyst derivatives

Table 1 Electrochemical data derived from cyclic voltammetry of 1 mM catalysts solutions in 0.1 M [Bu$_4$N][PF$_6$] acetonitrile electrolyte under 1 atm of argon at a glassy carbon disc working electrode. All potentials were recorded at υ = 0.1 V s^{-1} and are reported *versus* the ferricenium/ferrocene (Fc$^{+/0}$) redox couple

	E_{pa} [a]	E_{pa} [b]	E_{pc} [c]	E_{pc} [d]
[1-CH$_3$CN]$^+$	+1.00	−1.50	−1.55	−2.78
[2-CH$_3$CN]$^+$	+1.04	−1.52	−1.55	−2.85
[3-CH$_3$CN]$^+$	+0.73	−1.51	−1.56	−2.48
[4-CH$_3$CN]$^+$	+0.82	−1.50	−1.54	−1.90, −2.28, −2.80

[a] Irreversible Mn(I/II). [b] Oxidation of the two-electron reduced [Mn]$^-$ species. [c] Two-electron reduction. [d] Irreversible.

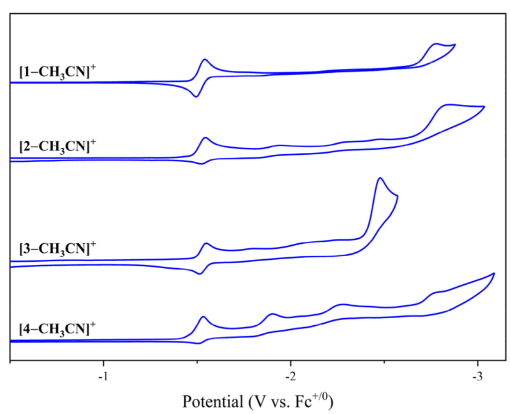

Fig. 2 Cyclic voltammograms of 1 mM **[1-CH$_3$CN]$^+$**, **[2-CH$_3$CN]$^+$**, **[3-CH$_3$CN]$^+$** and **[4-CH$_3$CN]$^+$** recorded in argon-saturated 0.1 M [Bu$_4$N][PF$_6$] acetonitrile supporting electrolyte at a glassy carbon electrode with a scan rate of 0.1 V s^{-1}.

confirming an ECE activation mechanism (eqn (1)–(3)). Unfortunately, the quality of IRSEC spectra was poor due to reduced solubility of all reduction products for each pre-catalyst. For this reason, identification of **[3-CH$_3$CN]^0** and **[4-CH$_3$CN]^0** was not feasible. Exemplar IRSEC spectra are provided in Fig. 3 for the *N*-boc-ala functionalized pre-catalyst **[2-CH$_3$CN]$^+$**.

Initial electrolysis of **[2-CH$_3$CN]$^+$** at −1.53 V exhibits depletion of the parent complex at 2043 and 1957 cm^{-1} with concurrent grow-in of the one-electron reduced six-coordinate species **[2-CH$_3$CN]^0** at 2023, 1931 and 1910 cm^{-1} (eqn (1)). Weak evidence of the two-electron reduced species **[2]$^-$** appeared to grow-in over an extended electrolysis time at 1807 cm^{-1}. Quantitative formation of **[2]$^-$** was observed at 1895 and 1807 cm^{-1} by applying a more negative potential of −2.00 V. A weak depletion of the parent *N*-boc ν(C═O) stretches was also observed upon formation of **[2]$^-$**, however this region of the spectrum was mostly obscured by strong electrolyte absorption. Comparable IRSEC results were recorded for all four complexes (Table 2) and is provided in the ESI (Fig. 25–27†).

Voltammetry under 1 atm CO$_2$ with Brønsted acid

Each catalyst was studied under 1 atm CO$_2$ in the presence of optimum H$_2$O and PhOH. Brønsted acid titration experiments were performed to determine the concentration of each acid at which proton dependence would not be rate-limiting. Furthermore, once optimum Brønsted acid concentrations were reached, scan rate dependence experiments were performed to reach steady-state conditions at which CO$_2$ consumption is also not rate-limiting to allow determination of the maximum turnover frequencies (TOF$_{max}$). The turnover frequency was determined using the ratio of catalytic current (i_{cat}) and non-catalytic faradaic current (i_p) according to eqn (6)

$$\mathrm{TOF} = \frac{F\upsilon {n_p}^3}{RT}\left(\frac{0.4463}{n_{cat}}\right)^2\left(\frac{i_{cat}}{i_p}\right)^2 \quad (6)$$

where F is the Faraday constant (96 485 s A mol^{-1}), υ is the scan rate (V s^{-1}), R is the universal gas constant (8.3145 V A s K^{-1} mol^{-1}), T is the temperature (298 K).[63] The first reduction wave was used as a reference point for both i_p and n_p (*i.e.* n_p = 2 for a two electron reduction). The number of electrons required for a single catalytic cycle is equivalent for each of the CO, HCO$_2^-$ and H$_2$ producing catalytic cycles (*i.e.* n_{cat} = 2). The maximum turnover frequency (TOF$_{max}$) was estimated by plotting TOF *vs.* scan rate.

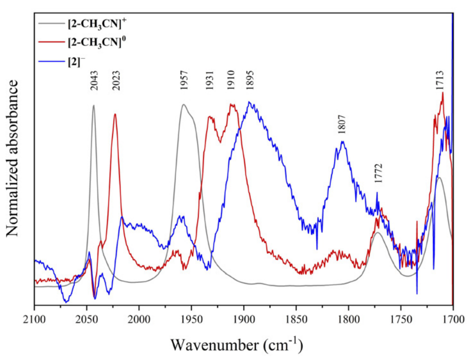

Fig. 3 IRSEC results upon controlled potential electrolysis of **[2-CH$_3$CN]$^+$** recorded in argon-saturated 0.1 M [Bu$_4$N][PF$_6$] acetonitrile supporting electrolyte.

Table 2 IRSEC-derived FTIR absorption data recorded in 0.1 M [Bu$_4$N][PF$_6$] acetonitrile electrolyte for all complexes, summarizing ν(CO) stretching frequencies

	ν(CO) cm^{-1}
[1-CH$_3$CN]$^+$	2043, 1958, 1949(sh), 1768^a, 1752(sh)^a
[1-CH$_3$CN]^0	2023, 1925
[1]$^-$	1911, 1812
[2-CH$_3$CN]$^+$	2043, 1957, 1772^a, 1713^a
[2-CH$_3$CN]^0	2023, 1931, 1910
[2]$^-$	1895, 1807
[3-CH$_3$CN]$^+$	2043, 1957, 1747^a, 1729(sh)^a
[3]$^-$	1912, 1808
[4-CH$_3$CN]$^+$	2044, 1958, 1948(sh), 1769^a, 1755(sh)^a
[4]$^-$	1913, 1813

^{a} Low energy ligand ν(C═O) absorption bands are obscured by strong electrolyte absorption for one- and two-electron reduced species in IRSEC experiments.

As discussed above, all four catalysts are activated by a two-electron reduction to the five coordinate 18-electron [Mn]$^-$ anions, primed for CO$_2$ and/or proton binding to form the key [Mn–CO$_2$H] and [Mn–H] intermediates. Optimum voltammetry at υ = 0.1 V s^{-1} for all four catalysts comparing both H$_2$O and PhOH proton sources is summarized in Table 4 below and illustrated in Fig. 4. Two catalytic waves grow-in in the presence of optimum PhOH (1.5 M) as the proton source. Consistent with our prior studies using a bulky proton donor, growth of the low-overpotential protonation-first pathway appears to be most prominent for **[1-CH$_3$CN]$^+$** and **[2-CH$_3$CN]$^+$**, which arguably possess lesser steric bulk.

Controlled potential electrolysis

To probe the product selectivity of each catalyst, controlled potential electrolysis (CPE) experiments were conducted at $E_{cat/2}$ of each catalytic wave under 1 atm CO$_2$ in the presence of an optimum concentration of H$_2$O or PhOH Brønsted acid proton sources. A summary of CPE parameters and faradaic yields is presented below in Table 3.

Of the four catalysts investigated only the simple methyl-ester second coordination sphere functional group in **[1-CH$_3$CN]$^+$** maintains a high selectivity for CO production across all CPE experimental conditions. Specifically, **[1-CH$_3$CN]$^+$** exhibits FE$_{CO}$ = 99% at high-overpotential ($E_{cat/2}$ = −1.96 V) in the presence of 6.0 M H$_2$O. In the presence of just 1.5 M PhOH, **[1-CH$_3$CN]$^+$** exhibits FE$_{CO}$ = 97% and 100% at its low overpotential ($E_{cat/2}$ = −1.55 V) and high overpotential ($E_{cat/2}$ = −1.93 V) catalytic waves, respectively. With such high selectivity for CO production the low and high overpotential catalytic waves of **[1-CH$_3$CN]$^+$** can be definitively attributed to the PT-ET (aka pro-

Table 4 Summary of electrocatalysis data derived from linear sweep voltammogram experiments for both low and high overpotential pathways

		$[1\text{-}CH_3CN]^+$		$[2\text{-}CH_3CN]^+$		$[3\text{-}CH_3CN]^+$		$[4\text{-}CH_3CN]^+$	
		H_2O	PhOH	H_2O	PhOH	H_2O	PhOH	H_2O	PhOH
Low η	$E_{cat/2}$ (V)	—	−1.55	—	−1.51	−1.47	−1.50	—	−1.45
	[HA] (M)	—	1.5	—	1.8	6.0	1.5	—	1.5
	TOF_{max} (s^{-1})	—	58	—	35	6	5	—	82
High η	$E_{cat/2}$ (V)	−1.96	−1.93	−1.96	−1.94	−1.96	−2.25	−1.92	−1.93
	[HA] (M)	6.0	1.5	6.4	1.8	6.0	1.5	6.0	1.5
	TOF_{max} (s^{-1})	167	235	127	598	78	10 451	586	1846

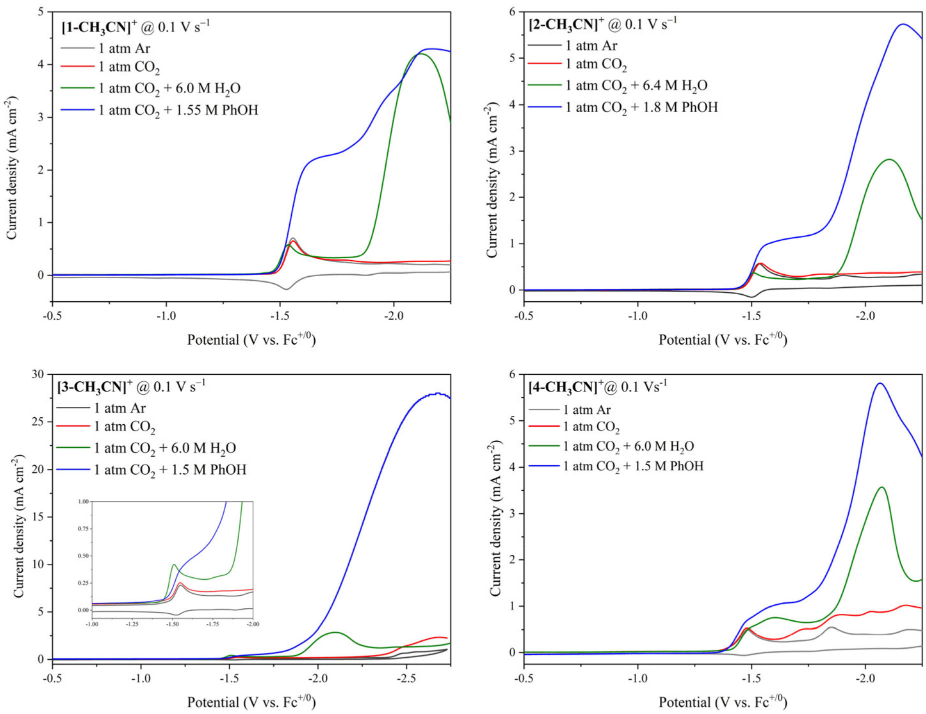

Fig. 4 Linear sweep voltammetry of all four complexes recorded at 1 mM concentration in 0.1 M $[Bu_4N][PF_6]$ acetonitrile electrolyte. Each plot includes cyclic voltammetry under 1 atm Ar, overlaid with linear sweep voltammetry in CO_2 saturated electrolyte with the addition of optimum concentrations of H_2O and PhOH.

tonation-first) and ET-PT (aka reduction-first) pathways of the CO_2-to-CO conversion catalytic cycle (re. Scheme 2 below). This observation further emphasizes the unique capacity of an *o*-aryl aprotic O-atom Brønsted base at promoting the highly desired low-overpotential PT-ET pathway for CO_2-to-CO conversion by Mn polypyridyl electrocatalysts.[58]

Discussion

To correctly discern the data here presented the relevant competing catalytic pathways exhibited by the Mn polypyridyl class of CO_2 reduction electrocatalysts must first be fully appreciated. Presented below are the established low- and high-overpotential catalytic pathways for each of the CO, HCO_2^- and H_2 products generated from the two-electron activated catalyst $[Mn]^-$; for brevity the core five-coordinate [*fac*-$Mn(R_2bpy)(CO)_3$] structure is abbreviated as [Mn] with [Mn–X] indicating the variable sixth coordination site throughout the catalytic cycle (Scheme 2). Formal Mn and R_2bpy oxidation states throughout the catalytic cycle are also illustrated in Scheme 2. The CO producing pathways originate from CO_2 binding to the active catalyst $[Mn]^-$, in the presence of a proton source, to generate the metallocarboxylic acid intermediate $[Mn\text{–}CO_2H]^0$. This intermediate may directly undergo rate-determining proton induced C–OH bond cleavage to evolve H_2O alongside the $[Mn^I\text{–}CO]^+$ cation. Reduction of this cation to $[Mn^I\text{–}CO]^0$ requires a potential less negative than initial catalyst activation, hence the onset of catalytic current for this low-overpotential PT-ET (aka protonation-first) pathway for CO evolution being coincident with the concerted two-electron catalyst activation reduction wave. The corresponding high-overpotential

Table 3 Summary of controlled potential electrolysis data. Experimental conditions: 5 mL of 1 mM catalyst in 0.1 M $[Bu_4N][PF_6]$ acetonitrile supporting electrolyte with optimum H_2O and PhOH concentrations under 1 atm CO_2

	HA[a] (M)	$E_{applied}$ (V *vs.* $Fc^{+/0}$)	Faradaic yield CO : HCO_2^- : H_2 (%)
[1-CH$_3$CN]$^+$	H_2O (6.0 M)	−1.96	99 : 0 : 1
	PhOH (1.5 M)	−1.55	97 : 0 : 1
	PhOH (1.5 M)	−1.93	100 : 0 : 0
[2-CH$_3$CN]$^+$	H_2O (6.4 M)	−1.96	42 : 48 : 1
	PhOH (1.8 M)	−1.51	100 : 0 : 0
	PhOH (1.8 M)	−1.94	54 : 43 : 1
[3-CH$_3$CN]$^+$	H_2O (6.0 M)	−1.60[b]	4 : 12 : 20
	H_2O (6.0 M)	−1.96	16 : 25 : 58
	PhOH (1.5 M)	−1.50	32 : 19 : 7
	PhOH (1.5 M)	−2.25	14 : 17 : 67
[4-CH$_3$CN]$^+$	H_2O (6.0 M)	−1.92	63 : 0 : 36
	PhOH (1.5 M)	−1.60[b]	66 : 0 : 12
	PhOH (1.5 M)	−1.93	59 : 0 : 34

[a] Refers to the concentration of Brønsted acid [HA] not be confused with [H$^+$]. [b] $E_{applied}$ was taken from the peak maximum due to the weak catalytic current.

ET-PT (aka reduction-first) CO producing pathway exhibits an onset of catalytic current at higher overpotential concomitant with one-electron reduction of the metallocarboxylic acid intermediate to generate the $[Mn–CO_2H]^-$ anion. Rate-determining proton induced C–OH bond cleavage at the $[Mn–CO_2H]^-$ anion is more facile hence the consistently higher catalytic rates for this ET-PT pathway relative to is low-overpotential PT-ET pathway. Should protonation of the $[Mn]^-$ active catalyst be favoured over CO_2 binding, $[Mn–H]^0$ is formed initiating entry to the competing HCO_2^- and H_2 evolving pathways. CO_2 insertion can occur, prior to reduction, along the low-overpotential (insert-ET) pathway, with an overpotential dictated by the $[Mn–CO_2H]^{0/-}$ reduction potential. Alternatively, the high-overpotential HCO_2^- producing pathway has an overpotential dictated by the $[Mn–H]^{0/-}$ reduction, followed by CO_2 insertion (ET-insert). The low-overpotential insert-ET formate pathway is kinetically inferior but has the advantage of eliminating competitive H_2 production relative to protonation of the anionic $[Mn–H]^-$ intermediate along the ET-insert pathway. It should also be noted that bimolecular H_2 production is known to occur from two equivalents of the neutral $[Mn–H]^0$ intermediate, at least with the non-sterically hindered bpy ligand.[12]

The first take away from this study is how the simplest *o*-arylester second coordination sphere functionality in pre-catalyst **[1-CH$_3$CN]$^+$** exhibits a rare example of the highly sought after low overpotential PT-ET catalytic pathway for selective CO production. However, despite the presence of an optimized PhOH concentration (1.5 M), the TOF_{max} values for both its low overpotential PT-ET (TOF_{max} = 58 s^{-1}, $E_{cat/2}$ = −1.55 V) and high overpotential ET-PT (TOF_{max} = 235 s^{-1}, $E_{cat/2}$ = −1.93 V) CO producing pathways are relatively low in comparison to our previously reported *o*-arylether analogues. That being said, the goal of this study was primarily to probe the impact of extending this second coordination sphere functionality on catalyst performance from the perspective of thermodynamics, kinetics and selectivity.

Second coordination sphere extension with the *N*-boc arylester system in pre-catalyst **[2-CH$_3$CN]$^+$** also exhibits highly selective CO production at low overpotential consistent with the PT-ET pathway in the presence of 1.8 M PhOH (TOF_{max} = 35 s^{-1}, $E_{cat/2}$ = −1.51 V). The slight reduction in catalytic rate relative to **[1-CH$_3$CN]$^+$** is likely due to steric bulk and crowding of the catalyst active site. Intriguingly, however, at higher overpotential ($E_{cat/2}$ = −1.94 V) under otherwise identical conditions this same catalyst exhibits an almost equal faradaic

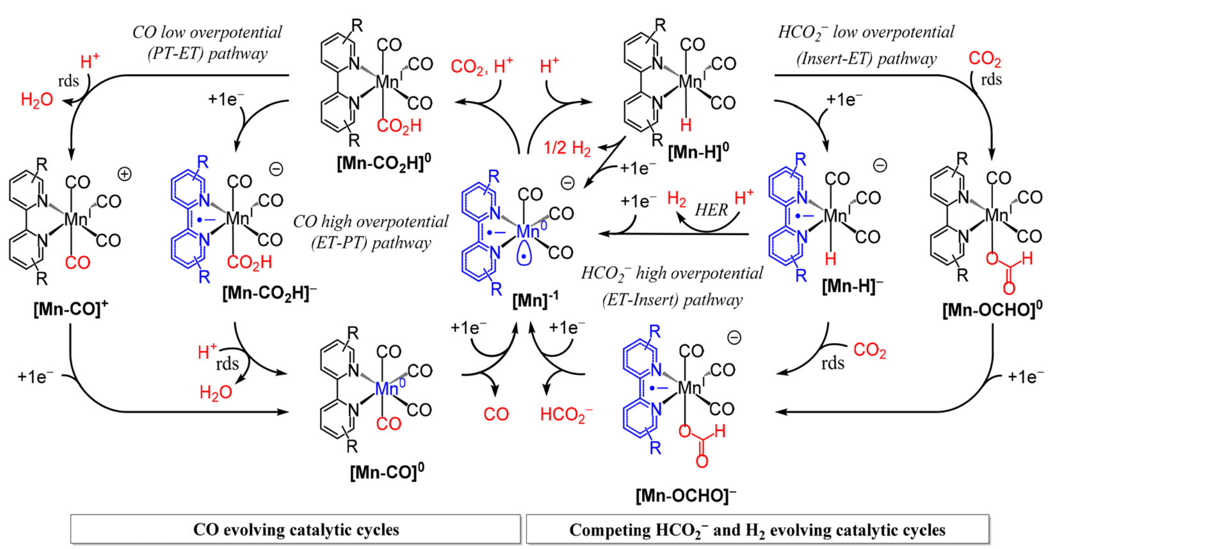

Scheme 2 A summary of competing catalytic pathways exhibited by the Mn polypyridyl class of CO_2 reduction electrocatalysts for CO, HCO_2^- and H_2 production. Left side: Low-overpotential (PT-ET) and high-overpotential (ET-PT) CO evolving pathways. Right side: Low-overpotential (insert-ET) and high-overpotential (ET-insert) pathways for HCO_2^- production, and competing hydrogen evolution reaction (HER) pathways.

yield for HCO_2^- production with negligible evidence for H_2 evolution. This suggests an almost 1 : 1 split with respect to the selectivity of the activated catalyst **[2]**$^-$ at binding CO_2 or H^+ to form the critical metallocarboxylic acid **[2-CO₂H]** or metal-hydride **[2-H]** intermediates along the CO or HCO_2^- *vs.* H_2 catalytic pathways (Scheme 2). **[2-CH₃CN]**$^+$ exhibits a very similar product distribution of $FE_{CO:HCO_2^-:H_2} = 42:1:48\%$ in the presence of optimum H_2O (6.4 M) at high overpotential ($E_{cat/2}$ = −1.96 V). Of great significant for each of these high overpotential observations of equitable CO *vs.* HCO_2^- formation is the negligible production of H_2. As the high-overpotentials required are consistent with HCO_2^- production along the ET-insert pathway, *via* the one-electron reduced manganese hydride intermediate **[2-H]**$^-$, this suggests that the *N*-boc terminated *o*-arylester second coordination sphere of **[2-CH₃CN]**$^+$ favors CO_2 insertion over protonation of **[2-H]**$^-$ to maintain a high selectivity for HCO_2^- production. This observation is indeed consistent with related complexes which also contain pendant amino functionalities in their SCS.[19,22,48] Estimated hydricities of the neutral [Mn–H] catalyst, using Kubiak's linear correlation method with two-electron reduction potentials, of all four complexes are in the range of $\Delta G^\circ_{H^-} \sim 46-47$ kcal mol^{-1}.[64] This is slightly endergonic of the 44 kcal mol^{-1} assumed necessary for HCO_2^- formation and may also explain the low yields of H_2 at low overpotential. Hydricity of the reduced [Mn–H]$^-$ intermediate has been estimated at ∼14 kcal mol^{-1} for a catalyst that exhibited 71% HCO_2^- selectivity and which bears pendant amine second coordination sphere, comparable in many respects to **[2-CH₃CN]**$^+$.[48]

In contrast, the decreased selectivity imparted by the *o*-methoxybenzoate second coordination sphere in **[3-CH₃CN]**$^+$ relative to the *N*-boc arylester in **[2-CH₃CN]**$^+$, in the presence of either PhOH or H_2O, is striking. It is also worth noting the more negative $E_{cat/2}$ of the large high-overpotential catalytic wave of **[3-CH₃CN]**$^+$ at −2.25 V in the presence of PhOH. Considering how the three-electron reduced derivative may be accessed at E_{pc} = −2.48 V (Table 1) this contrasting reactivity could possibly be associated with a three-electron activated catalyst thereby mitigating any desired control of product selectivity. However, an alternative explanation may be that the product selectivity of **[3-CH₃CN]**$^+$ is simply dictated by the steric bulk of the extended second coordination sphere structure with limited influence of the second coordination sphere.[57] Controlled potential electrolysis studies of the bulky **[4-CH₃CN]**$^+$ catalyst do indicate that CO_2 binding is favoured but significant H_2 evolution is still observed in this case. Although computed transition state geometries suggest the Mn active site is accessible in the *syn*,*anti* atropisomers of **[3-CH₃CN]**$^+$ and **[4-CH₃CN]**$^+$ (ESI Fig. 42–47†), not knowing the ratio of atropisomers in solution prevents any real conclusions to be made at this time with respect to the balance of steric *vs.* second coordination sphere effects on their product distribution.

To further investigate the influence of extended functionality at the second-coordination sphere, we performed density functional theory (DFT) calculations at the MN15 level of theory in conjunction with the SMD continuum solvation model for acetonitrile. For computational efficiency only the *syn*,*anti* atropisomers were calculated, and the terminal *tert*-butyl substituents of the *N*-boc protecting groups were modelled as methyl groups (see Computational methods in the ESI† for details). Using theory to predict product selectivities at high overpotential is extremely challenging due to the competition between several pathways leading to CO, HCO_2^- and H_2 production. This is further compounded by the unknown ratio of atropisomers in each CPE experiment which likely exhibit varying product distributions. Thus, our primary aim in utilizing theoretical calculations in this work focussed on a qualitative assessment for the disparate product selectivities of just **[2-CH₃CN]**$^+$ and **[3-CH₃CN]**$^+$. The energetics of their transition state structures for **[Mn–CO₂]**$^-$ and **[Mn–H]** formation, and Insert-ET *versus* ET-insert pathways for HCO_2^- and H_2 production, were analyzed. The free energy of activation ($\Delta G^\ddagger$) values, assuming fully separated reactants in solution, are illustrated in Fig. 5 for **[2-CH₃CN]**$^+$, (for tabulated data *vs.* **[3-CH₃CN]**$^+$ see ESI Table 1†).

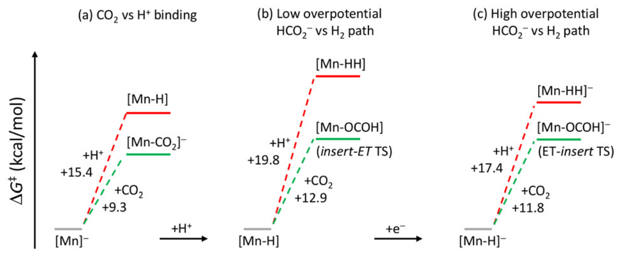

Fig. 5 A comparison of relative free energies of activation ($\Delta G^\ddagger$) values in kcal mol^{-1} for selected kinetic steps in Scheme 2 for **[2-CH₃CN]**$^+$ with PhOH as the Brønsted acid source.

The computed $\Delta G^\ddagger$s indicate that CO_2 binding to doubly reduced **[2]**$^-$ is significantly favored over protonation by PhOH to generate **[2-H]**, however, the activation enthalpies (ESI Table 1,† $\Delta H^\ddagger$) are nearly isothermic which is more consistent with the almost equal product distribution of CO : HCO_2^- in controlled potential electrolysis. Once the **[2-H]**$^-$ intermediate is formed, HCO_2^- formation by electrophilic attack of CO_2 is favored over H_2 formation in line with our experimental observations (Fig. 5c). Theoretical data for **[3-CH₃CN]**$^+$ was inconsistent with our CPE experiments, however, as pointed out earlier, this may likely be due to three-electron activation of pre-catalyst **[3-CH₃CN]**$^+$ leading to excessive H_2 production, or alternatively steric crowding of the active site hindering CO_2 binding at **[3]**$^-$ or insertion at **[3-H]**$^-$ thereby enhancing the H_2 yield.

Conclusions

This study demonstrates that the introduction of distal, outer coordination sphere, H-bonding functionality at the periphery of a homogeneous transition metal complex active site, can have a strong influence on product selectivity for proton-coupled electrocatalytic CO_2 reduction. Although the bulky *o*-methoxybenzoate group diminishes the product selectivity for CO_2 reduction, extension of the CO selective acetate SCS with the tertiary amine *N*-Boc-ala group shifts the reaction pathway toward a 1 : 1 ratio of the [Mn–CO_2H] and [Mn–H] intermediates with a surprising selectivity for CO_2 insertion at [Mn–H] along the competing HCO_2^- *vs.* H_2 pathways as corroborated by computational studies.

Author contributions

The manuscript was drafted through the contributions of all authors: L. S., V. B. and R. S. experimental studies and data analysis; M. Z. E. computational analysis; J. R. data analysis, L. S., V. B. and R. S. supervision and project management.

Data availability

The data supporting this article have been included as part of the ESI.†

Conflicts of interest

There are no conflicts to declare.

Acknowledgements

JR thanks the National Science Foundation for support under Grant No. CHE-1800062. The work at Brookhaven National Laboratory (M. Z. E.) was carried out under contract DE-SC0012704 with the U.S. Department of Energy, Office of Science, Office of Basic Energy Sciences, and utilized computational resources at the Center for Functional Nanomaterials, which is a U.S. DOE Office of Science Facility, and the Scientific Data and Computing Center, a component of the Computational Science Initiative, at Brookhaven National Laboratory under Contract No. DE-SC0012704.

References

1 H. Takeda, C. Cometto, O. Ishitani and M. Robert, *ACS Catal.*, 2017, **7**, 70–88.
2 A. M. Appel, J. E. Bercaw, A. B. Bocarsly, H. Dobbek, D. L. DuBois, M. Dupuis, J. G. Ferry, E. Fujita, R. Hille, P. J. A. Kenis, C. A. Kerfeld, R. H. Morris, C. H. F. Peden, A. R. Portis, S. W. Ragsdale, T. B. Rauchfuss, J. N. H. Reek, L. C. Seefeldt, R. K. Thauer and G. L. Waldrop, *Chem. Rev.*, 2013, **113**, 6621–6658.
3 F. Franco, C. Rettenmaier, H. S. Jeon and B. Roldan Cuenya, *Chem. Soc. Rev.*, 2020, **49**, 6884–6946.
4 A. W. Nichols and C. W. Machan, *Front. Chem.*, 2019, **7**, 397.
5 S. Amanullah, P. Saha, A. Nayek, M. E. Ahmed and A. Dey, *Chem. Soc. Rev.*, 2021, **50**, 3755–3823.
6 S. Sinha, C. K. Williams and J. Jiang, *iScience*, 2022, **25**, 103628.
7 S. T. Stripp, B. R. Duffus, V. Fourmond, C. Léger, S. Leimkühler, S. Hirota, Y. L. Hu, A. Jasniewski, H. Ogata and M. W. Ribbe, *Chem. Rev.*, 2022, **122**, 11900–11973.
8 M. Rakowski DuBois and D. L. DuBois, *Chem. Soc. Rev.*, 2009, **38**, 62–72.
9 S. K. Mandal, S. Ray and J. Choudhury, *ChemCatChem*, 2024, **16**, e202401149.
10 S. Diyali, N. Diyali and B. Biswas, *Coord. Chem. Rev.*, 2024, **500**, 215496.
11 J. P. Collin, A. Jouaiti and J. P. Sauvage, *Inorg. Chem.*, 1988, **27**, 1986–1990.
12 D. C. Grills, Y. Matsubara, Y. Kuwahara, S. R. Golisz, D. A. Kurtz and B. A. Mello, *J. Phys. Chem. Lett.*, 2014, **5**, 2033–2038.
13 W. W. Kramer and C. C. L. McCrory, *Chem. Sci.*, 2016, **7**, 2506–2515.
14 J. Honores, D. Quezada, M. García, K. Calfumán, J. P. Muena, M. J. Aguirre, M. C. Arévalo and M. Isaacs, *Green Chem.*, 2017, **19**, 1155–1162.
15 E. M. Nichols, J. S. Derrick, S. K. Nistanaki, P. T. Smith and C. J. Chang, *Chem. Sci.*, 2018, **9**, 2952–2960.
16 E. M. Nichols and C. J. Chang, *Organometallics*, 2019, **38**, 1213–1218.
17 P. Gotico, B. Boitrel, R. Guillot, M. Sircoglou, A. Quaranta, Z. Halime, W. Leibl and A. Aukauloo, *Angew. Chem., Int. Ed.*, 2019, **58**, 4504–4509.
18 Y. Liu and C. C. L. McCrory, *Nat. Commun.*, 2019, **10**, 1683.
19 M. Bhattacharya, S. Sebghati, R. T. VanderLinden and C. T. Saouma, *J. Am. Chem. Soc.*, 2020, **142**, 17589–17597.
20 C. K. Williams, A. Lashgari, J. Chai and J. J. Jiang, *ChemSusChem*, 2020, **13**, 3412–3417.
21 Y. S. Liu, A. Deb, K. Y. Leung, W. X. Nie, W. S. Dean, J. E. Penner-Hahn and C. C. L. McCrory, *Dalton Trans.*, 2020, **49**, 16329–16339.
22 M. R. Madsen, M. H. Rønne, M. Heuschen, D. Golo, M. S. G. Ahlquist, T. Skrydstrup, S. U. Pedersen and K. Daasbjerg, *J. Am. Chem. Soc.*, 2021, **143**, 20491–20500.
23 H. J. Dai, R. Cui, C. S. Chen, J. T. Song, J. H. Li, L. Z. Dong, C. Y. Yu, W. F. Jiang and Y. F. Zhou, *Chem. – Eur. J.*, 2023, **29**, e202300879.
24 K. Teindl, B. O. Patrick and E. M. Nichols, *J. Am. Chem. Soc.*, 2023, **145**, 17176–17186.
25 S. Patra, S. Bhunia, S. Ghosh and A. Dey, *ACS Catal.*, 2024, **14**, 7299–7307.
26 J. T. Bays, N. Priyadarshani, M. S. Jeletic, E. B. Hulley, D. L. Miller, J. C. Linehan and W. J. Shaw, *ACS Catal.*, 2014, **4**, 3663–3670.
27 A. P. Walsh, J. A. Laureanti, S. Katipamula, G. M. Chambers, N. Priyadarshani, S. Lense, J. T. Bays, J. C. Linehan and W. J. Shaw, *Faraday Discuss.*, 2019, **215**, 123–140.
28 A. Dubey, L. Nencini, R. R. Fayzullin, C. Nervi and J. R. Khusnutdinova, *ACS Catal.*, 2017, **7**, 3864–3868.

29 D. Wei, R. Sang, P. Sponholz, H. Junge and M. Beller, *Nat. Energy*, 2022, **7**, 438–447.
30 L. K. Oliemuller, C. E. Moore and C. M. Thomas, *Inorg. Chem.*, 2023, **62**, 13997–14009.
31 S. Kostera, G. Manca and L. Gonsalvi, *Chem. – Eur. J.*, 2023, **29**, e202302642.
32 S. Kostera and L. Gonsalvi, *ChemCatChem*, 2024, **16**, e202301391.
33 A. Dutta, S. Lense, J. Hou, M. H. Engelhard, J. A. S. Roberts and W. J. Shaw, *J. Am. Chem. Soc.*, 2013, **135**, 18490–18496.
34 G. Marcandalli, M. C. O. Monteiro, A. Goyal and M. T. M. Koper, *Acc. Chem. Res.*, 2022, **55**, 1900–1911.
35 X. Li and J. J. Warren, *Dalton Trans.*, 2025, **54**, 2086–2092.
36 J. S. Derrick, M. Loipersberger, S. K. Nistanaki, A. V. Rothweiler, M. Head-Gordon, E. M. Nichols and C. J. Chang, *J. Am. Chem. Soc.*, 2022, **144**, 11656–11663.
37 W. W. Kramer and C. C. L. McCrory, *Chem. Sci.*, 2016, **7**, 2506–2515.
38 F. Franco, C. Cometto, F. F. Vallana, F. Sordello, E. Priola, C. Minero, C. Nervi and R. Gobetto, *Chem. Commun.*, 2014, **50**, 14670–14673.
39 C. W. Machan, S. A. Chabolla, J. Yin, M. K. Gilson, F. A. Tezcan and C. P. Kubiak, *J. Am. Chem. Soc.*, 2014, **136**, 14598–14607.
40 J. Agarwal, T. W. Shaw, H. F. Schaefer III and A. B. Bocarsly, *Inorg. Chem.*, 2015, **54**, 5285–5294.
41 C. W. Machan and C. P. Kubiak, *Dalton Trans.*, 2016, **45**, 15942–15950.
42 F. Franco, C. Cometto, L. Nencini, C. Barolo, F. Sordello, C. Minero, J. Fiedler, M. Robert, R. Gobetto and C. Nervi, *Chem. – Eur. J.*, 2017, **23**, 4782–4793.
43 K. T. Ngo, M. McKinnon, B. Mahanti, R. Narayanan, D. C. Grills, M. Z. Ertem and J. Rochford, *J. Am. Chem. Soc.*, 2017, **139**, 2604–2618.
44 E. Haviv, D. Azaiza-Dabbah, R. Carmieli, L. Avram, J. M. L. Martin and R. Neumann, *J. Am. Chem. Soc.*, 2018, **140**, 12451–12456.
45 S. Sung, X. H. Li, L. M. Wolf, J. R. Meeder, N. S. Bhuvanesh, K. A. Grice, J. A. Panetier and M. Nippe, *J. Am. Chem. Soc.*, 2019, **141**, 6569–6582.
46 L. Rotundo, D. E. Polyansky, R. Gobetto, D. C. Grills, E. Fujita, C. Nervi and G. F. Manbeck, *Inorg. Chem.*, 2020, **59**, 12187–12199.
47 K. Talukdar, S. S. Roy, E. Amatya, E. A. Sleeper, P. Le Magueres and J. W. Jurss, *Inorg. Chem.*, 2020, **59**, 6087–6099.
48 M. H. Rønne, D. Cho, M. R. Madsen, J. B. Jakobsen, S. Eom, É. Escoudé, H. C. D. Hammershøj, D. U. Nielsen, S. U. Pedersen, M.-H. Baik, T. Skrydstrup and K. Daasbjerg, *J. Am. Chem. Soc.*, 2020, **142**, 4265–4275.
49 M. R. Madsen, J. B. Jakobsen, M. H. Ronne, H. Liang, H. C. D. Hammershoj, P. Norby, S. U. Pedersen, T. Skrydstrup and K. Daasbjerg, *Organometallics*, 2020, **39**, 1480–1490.
50 S. S. Roy, K. Talukdar and J. W. Jurss, *ChemSusChem*, 2021, **14**, 662–670.
51 X. H. Li and J. A. Panetier, *Phys. Chem. Chem. Phys.*, 2021, **23**, 14940–14951.
52 Y. Yang, M. Z. Ertem and L. L. Duan, *Chem. Sci.*, 2021, **12**, 4779–4788.
53 M. H. Ronne, M. R. Madsen, T. Skrydstrup, S. U. Pedersen and K. Daasbjerg, *ChemElectroChem*, 2021, **8**, 2108–2114.
54 L. Rotundo, D. C. Grills, R. Gobetto, E. Priola, C. Nervi, D. E. Polyansky and E. Fujita, *ChemPhotoChem*, 2021, **5**, 526–537.
55 S. S. Roy, K. Talukdar, S. T. Sahil and J. W. Jurss, *Polyhedron*, 2022, **224**, 115976.
56 V. Blasczak, M. McKinnon, L. Suntrup, N. A. Aminudin, B. Reed, S. Groysman, M. Z. Ertem, D. C. Grills and J. Rochford, *Inorg. Chem.*, 2022, **61**, 15784–15800.
57 W. W. Hong, M. Luthra, J. B. Jakobsen, M. R. Madsen, A. C. Castro, H. C. D. Hammershoj, S. U. Pedersen, D. Balcells, T. Skrydstrup, K. Daasbjerg and A. Nova, *ACS Catal.*, 2023, **13**, 3109–3119.
58 V. Blasczak, A. Murphy, L. Suntrup, K. T. Ngo, B. Reed, S. Groysman, D. C. Grills and J. Rochford, *ChemCatChem*, 2024, **16**, e202301388.
59 W. Hong, J. B. Jakobsen, D. Golo, M. R. Madsen, M. S. G. Ahlquist, T. Skrydstrup, S. U. Pedersen and K. Daasbjerg, *ChemElectroChem*, 2024, **11**, e202300553.
60 Y. Hiraga, S. Chaki, Y. Uyama, R. Hoshide, T. Karaki, D. Nagata, K. Yoshimoto and S. Niwayama, *Organics*, 2022, **3**, 38–58.
61 J. O. Taylor, Y. Wang and F. Hartl, *ChemCatChem*, 2020, **12**, 386–393.
62 M. D. Sampson, A. D. Nguyen, K. A. Grice, C. E. Moore, A. L. Rheingold and C. P. Kubiak, *J. Am. Chem. Soc.*, 2014, **136**, 5460–5471.
63 D. C. Grills, M. Z. Ertem, M. McKinnon, K. T. Ngo and J. Rochford, *Coord. Chem. Rev.*, 2018, **374**, 173–217.
64 K. M. Waldie, A. L. Ostericher, M. H. Reineke, A. F. Sasayama and C. P. Kubiak, *ACS Catal.*, 2018, **8**, 1313–1324.

